

Mapping H I 21-cm in the Klemola 31 group at $z = 0.029$: emission and absorption towards PKS 2020-370

E. K. Maina^{1*}, Abhisek Mohapatra,² G. I. G. Józsa,^{3,1} N. Gupta,² F. Combes,⁴ P. Deka,² J. D. Wagnveld,³ R. Srianand,² S. A. Balashev,^{5,6} Hsiao-Wen Chen,⁷ J.-K. Krogager,⁸ E. Momjian,⁹ P. Noterdaeme,^{10,11} and P. Petitjean¹⁰

¹Department of Physics and Electronics, Rhodes University, P.O. Box 94, Makhanda, 6140, South Africa

²Inter-University Centre for Astronomy and Astrophysics, Post Bag 4, Ganeshkhind, Pune 411 007, India

³Max-Planck-Institut für Radioastronomie, Auf dem Hügel 69, D-53121 Bonn, Germany

⁴Observatoire de Paris, LERMA, Collège de France, CNRS, PSL University, Sorbonne University, Paris, France

⁵Ioffe Institute, Politeknicheskaya 26, 194021 Saint Petersburg, Russia

⁶HSE University, Saint Petersburg, Russia

⁷Department of Astronomy & Astrophysics, The University of Chicago, 5640 South Ellis Avenue, Chicago, IL 60637, USA

⁸Université Lyon1, ENS de Lyon, CNRS, Centre de Recherche Astrophysique de Lyon UMR5574, F-69230 Saint-Genis-Laval, France

⁹National Radio Astronomy Observatory, P.O. Box 0, Socorro, NM 87801, USA

¹⁰Institut d'Astrophysique de Paris, Sorbonne Université and CNRS, 98bis boulevard Arago, F-75014 Paris, France

¹¹Franco-Chilean Laboratory for Astronomy, IRL 3386, CNRS and U. de Chile, Casilla 36-D, Santiago, Chile

Accepted XXX. Received YYY; in original form ZZZ

ABSTRACT

We present MeerKAT Absorption Line Survey (MALS) observations of the H I gas in the Klemola 31 galaxy group ($z = 0.029$), located along the line of sight to the radio-loud quasar PKS 2020-370 ($z = 1.048$). Four galaxies of the group are detected in H I emission, and H I absorption is also detected in front of PKS 2020-370 in Klemola 31A. The emission and absorption are somewhat compensating on the line of sight of the quasar, and the derived column density of the absorption appears under-estimated, with respect to the neighbouring emission. A symmetric tilted-ring model of Klemola 31A, assuming the absorbing gas in regular rotation in the plane, yields a rather high spin temperature of 530 K. An alternative interpretation is that the absorbing gas is extra-planar, which will also account for its non-circular motion. The Na I/Ca II ratio also suggests that the absorbing gas is unrelated to cold H I disk. Two of the galaxies in the Klemola group are interacting with a small companion, and reveal typical tidal tails, and velocity perturbations. Only one of the galaxies, ESO 400-13, reveals a strong H I deficiency, and a characteristic ram-pressure stripping, with a total asymmetry in the distribution of its gas. Since a small galaxy group as Klemola 31 is not expected to host a dense intra-group gas, this galaxy must be crossing the group at a very high velocity, mostly in the sky plane.

Key words: galaxies: evolution – galaxies: formation – galaxies: groups: individual – galaxies: haloes – galaxies: interactions – quasars: absorption lines.

1 INTRODUCTION

Atomic hydrogen or H I is a transitional phase of the most abundant atom in the universe. On its path from ionized to molecular hydrogen (H₂), the basic fuel for star formation, it must transit through a cool phase forming the cold neutral medium (CNM; $T \sim 100$ K). Thus, the CNM fraction of gas in a galaxy is expected to be related to the efficiency with which gas is converted into stars. On the other hand, the warmer circumgalactic gas, which eventually might fuel star formation, also has a neutral component, which can be traced us-

ing H I observations. Vice versa, gas in galaxies being ionized from feedback processes must also go through this phase and might be pushed into the outskirts of galaxies. H I is therefore also a tracer of gas depletion. Studies of H I in the interstellar and intergalactic medium are hence of utmost importance to understand the processes that govern galaxy formation and evolution.

In the nearby Universe, the H I 21-cm emission line observations can be used to map the distribution and kinematics of bulk neutral gas, i.e., regardless of the kinetic temperature of gas, associated with galaxies. H I 21-cm emission line observations are primarily limited by resolution effects and the column density detection limit increases with the distance. The

* E-mail: kamau757@gmail.com

availability of resolved H I 21-cm line imaging of large number of galaxies from the ongoing large survey projects with the Square Kilometer Array (SKA) precursor telescopes i.e., the Australian Square Kilometre Array Pathfinder (ASKAP) (Hotan et al. 2021) and MeerKAT (Jonas & MeerKAT Team 2016) offers an unprecedented opportunity to address these issues (e.g., Jarvis et al. 2016; Serra et al. 2016; Koribalski et al. 2020; Maddox et al. 2021). This is, however, with the exception of very deep observations providing a low-number statistics of resolved galaxies, mostly still restricted to a redshift range of $z < 0.1$. At higher redshift, the neutral gas can in turn be detected through H I 21-cm absorption whenever it lies between the observer and a strong background radio source. This technique, however, generally provides information along one sight line, albeit at a resolution defined by the angular size of the background radio continuum. Another important characteristic of this technique is that the strength of the H I 21-cm absorption is inversely proportional to the spin temperature (T_s) of the gas and, hence, more efficient in tracing the colder atomic phases (e.g., Kulkarni & Heiles 1988). H I 21-cm absorption and emission line observations therefore nicely complement each other.

To interpret H I absorption at higher redshift, it is important to conduct studies at lower redshift, where both emission and absorption signals are detectable. It is now well recognized that mergers and interactions with other galaxies, and ram pressure stripping due to hot gas in group and cluster environments, play an important role in defining the overall structure i.e., formation of arms and bars, and the gas content of galaxies (e.g., Dressler 1980; Gerin et al. 1990; Elmegreen et al. 1991; Irwin 1994; Yun et al. 1994; Cappellari et al. 2011; Reynolds et al. 2021; Wang et al. 2021; Castignani et al. 2022). These processes will feed the circumgalactic medium, and it is not yet quite clear which of these media is actually traced by H I absorption lines in general. The low-redshift H I 21-cm emission and absorption line observations can help in recognizing the processes dominating in different galaxy environments.

The large survey project *MeerKAT Absorption Line Survey* (MALS) is carrying out a sensitive dust-unbiased search of H I 21-cm and OH 18-cm absorption lines with a primary goal to better understand the evolution of cold atomic and molecular gas at $0 < z < 2$ (Gupta et al. 2016). Owing to the large field-of-view ($\sim 1^\circ$ at 1.4 GHz) and excellent sensitivity, MALS can also detect H I 21-cm line emission from nearby galaxies. The background radio loud AGN within the MALS pointing can then be used to simultaneously search for H I 21-cm absorption in galaxies and the associated environment. An excellent demonstration of this is presented by Boettcher et al. (2022) reporting the discovery of neutral gas detected in both damped Ly α absorption (DLA) and H I 21-cm emission outside of the stellar body of a dwarf galaxy, at a distance of 33 kpc from another dwarf galaxy. The interaction between these two dwarf galaxies is revealed by a bridge detected in H I emission, and the non-detection of H I 21-cm absorption shows that the gas producing DLA is warm ($T_s > 1880$ K) or clumpy. Overall, MALS offers obvious advantages of combining H I 21-cm emission and absorption line measurements in revealing the physical state and parsec-scale structure of atomic gas in nearby galaxies, which till now have been scarcely applied beyond the Milky Way (e.g.,

Carilli & van Gorkom 1992; Borthakur et al. 2014; Dutta et al. 2016; Reeves et al. 2016; Gupta et al. 2018).

In this work, we present a detailed H I 21-cm absorption and emission line study of the Klemola 31 galaxy group ($z_{grp} = 0.029$) in the foreground of a distant quasar, PKS 2020-370 (RA: 20:23:46.200, Dec -36:55:20.50 (J2000; Healey et al. 2008) at $z_q = 1.048$ (Peterson et al. 1976). The group consists of six galaxies and the quasar sightline passes through one of them i.e., Klemola 31A. Previously, detections of Ca II, K and H lines (Boksenberg et al. 1980) and a faint H I 21-cm absorption (Boisse et al. 1988; Carilli & van Gorkom 1987) have been reported in the literature. Through MeerKAT, we detect H I 21-cm emission from the galaxy group and absorption associated with Klemola 31A. We also complement the latter with the upgrade Giant Metrewave Radio Telescope (uGMRT).

This paper is organized as follows. In Section 2, we introduce the properties of Klemola 31 group. In Section 3, we present MeerKAT and uGMRT observations, and data analysis. In Section 4, we present details of the H I 21-cm emission line properties of the group followed by the H I 21-cm absorption line properties towards PKS 2020-370 and the implications. A summary of results is presented in Section 5. Throughout the paper, we use Λ CDM cosmology with $H_0 = 70 \text{ km s}^{-1} \text{ Mpc}^{-1}$, $\Omega_\Lambda = 0.7$, and $\Omega_m = 0.3$. At the distance of the Klemola 31 galaxy group ($z_{grp} = 0.029$), $1'' = 0.6 \text{ kpc}$.

2 KLEMOLA 31 GROUP

Klemola 31 is a small group of galaxies at $z_{grp} = 0.029$ located in the Sagittarius constellation in the southern hemisphere (Klemola 1969). The group consists of six galaxies with different masses, morphological types and gas distributions. The basic properties of the member galaxies are summarized in Table 1. The redshifts of five of the six member galaxies are based on the publicly available optical spectra from the 6dF Galaxy Survey (6dFGS)². In short, the redshifts of ESO 400-11 and LEDA 631562 are based on the prominent H α ($\lambda 6565 \text{ \AA}$) emission line. For the early type galaxies, ESO 400-13, Klemola 31B and LEDA 2807038, the Mg ($\lambda 5177 \text{ \AA}$) and Na ($\lambda 5896 \text{ \AA}$) absorption lines have been used. For Klemola 31A ($z_g = 0.0288$), which has no public spectra available, the redshift is taken from Boksenberg et al. (1980) and Carilli & van Gorkom (1987). With respect to Klemola 31A, the other members of the group are within an angular separation of $\sim 5'$, which corresponds to a projected distance of $\sim 176 \text{ kpc}$ at the mean redshift of the group, $z_{grp} = 0.029$ (see last column of Table 1). The background quasar PKS 2020-370 is at an angular separation of $18''.7$, i.e., 10 kpc at z_{grp} , from Klemola 31A.

Boisse et al. (1988) detected H I emission from the group using the Nancay radio telescope. The telescope beam covers four members of the group: Klemola 31A, Klemola 31B, ESO 400-11 and LEDA 2807038. Using the morphology and inclinations of these galaxies, Boisse et al. (1988) argued that the detected H I emission signal (integrated flux, $S = 0.78 \text{ Jy km s}^{-1}$) corresponds to Klemola 31A ($M_{H I} = 6 \times 10^9 h^{-2}$).

² <http://www.6dfigs.net/>

Table 1. List of galaxy members of Klemola 31 group.

Name	RA	DEC	z_g^\dagger	B mag [†]	D_{25}^\dagger	i_{opt}^\dagger	Morph. [†]	Angular separation	Impact parameter
(1)	(2)	(3)	(4)	(mag)	(kpc)	(7)	(8)	(arcmin)	(kpc)
(1)	(2)	(3)	(4)	(5)	(6)	(7)	(8)	(9)	(10)
ESO 400-11	20:23:36.81	-36:52:55.48	0.0284	15.79	42.7 ± 4.0	79°	Sc	2.75	96
ESO 400-13	20:24:01.94	-36:56:16.99	0.0292	14.98	41.6 ± 4.2	64°	S0	3.55	124
Klemola 31A	20:23:45.21	-36:55:05.87	0.0288	15.91	31.5 ± 3.9	68°	Sc	-	-
LED A 631562	20:24:06.06	-36:52:24.00	0.0292	16.52	21.5 ± 4.3	46°	Sbc*	5.06	176
Klemola 31B	20:23:50.06	-36:55:18.54	0.0286	16.80	19.2 ± 6.7	55°	E*	0.99	35
LED A 2807038	20:23:34.76	-36:53:15.31	0.0295	16.80	15.2 ± 6.3	39°	E*	2.79	97

Columns 1 – 3: Galaxy name, position i.e., right ascension and declination (J2000) from SIMBAD¹. Column 4: redshift of the galaxy obtained from the optical spectra of 6dF Galaxy Survey (6dFGS); for Klemola31A see [Boksenberg et al. \(1980\)](#) and ([Carilli & van Gorkom 1987](#)). Column 5: Total B-band magnitude. Column 6: the extinction-corrected optical diameter measured at the 25th mag arcsec⁻² isophote from HyperLeda. Column 7: inclination angle calculated from the axis ratio of the isophote at 25 mag arcsec⁻² in the B-band. Column 8: Morphological type of the galaxy. Column 9: Angular separation from Klemola 31A. Column 10: Projected distance from Klemola 31A using average redshift of the group, $z_{grp} = 0.0290$.

[†]from HYPERLEDA; * from visual classification based on the optical image.

Later, [Carilli & van Gorkom \(1992\)](#) using the Very Large Array (VLA of the NRAO³) in BnA and CnB configurations constrained the H I content of Klemola 31A and Klemola 31B to be $M_{H I} = 1.16 \times 10^9 h^{-2} M_\odot$ and $M_{H I} < 10^9 h^{-2} M_\odot$, respectively. For the H I mass upper limit they assumed a velocity width of 200 km s⁻¹.

Through the detection of Ca II K and H absorption lines at $z_{abs} = 0.0287$ in the spectra of PKS 2020-370 ([Boksenberg et al. 1980](#)), it has been known for a long time that gas extends well outside the optical disks / halos of Klemola 31A and Klemola 31B. The latter is at an angular separation of 45'' from the quasar sight line. The above mentioned H I 21-cm emission line observations subsequently showed the gas to be associated with the extended H I disk of Klemola 31A. [Junkkarinen & Barlow \(1994\)](#) detected Na I absorption lines and showed that the ratio $N(\text{Ca II})/N(\text{Na I})$ is rather consistent with the ‘halo-like’ gas (see also [Cherinka & Schulte-Ladbeck 2011](#)). Both [Boisse et al. \(1988\)](#) and [Carilli & van Gorkom \(1992\)](#) have reported the detections of H I 21-cm absorption from Klemola 31A. However, the best available constraint on integrated H I 21-cm optical depth ($\int \tau dv = 0.22 \pm 0.05 \text{ km s}^{-1}$) is based on VLA A-configuration observations (spectral resolution $\sim 10 \text{ km s}^{-1}$ per channel) that resolve out the extended H I emission signal ([Carilli & van Gorkom 1987](#)). This corresponds to a H I column density, $N(\text{H I}) = 4.0 \times 10^{19} (T_s/100 \text{ K}) \text{ cm}^{-2}$.

The availability of a variety of H I 21-cm emission and absorption line information motivated the use of Klemola group as target for MALS science verification observations.. At the same time, the H I 21-cm emission line properties of the other four members of the galaxy group i.e., ESO 400-11, LED A 2807038, LED A 631562 and ESO 400-13 have not been discussed at all in the literature, and the absorption signal towards PKS 2020-370 although unambiguously detected, albeit as a single pixel, is not well characterized due to the low spectral resolution. Thus, it is also an intriguing target to follow-up using the large field-of-view, excellent sensitivity

and high spectral resolution of MeerKAT observations presented here.

3 OBSERVATIONS AND ANALYSIS

3.1 MeerKAT

The pointing centered at PKS 2020-370 was observed on April 1, 2020 using 60 antennas of the MeerKAT-64 array and 32K mode of the SKA Reconfigurable Application Board (SKARAB) correlator. The total duration of these science verification observing run was 184 min. The total on-source time of 56 mins on PKS 2020-370 was split into three scans at different hour angles to improve the uv coverage. We observed 3C286 and PKS 1939-638 for flux density scale, delay and bandpass calibrations, and the compact radio source J2052-3640 was periodically observed for complex gain calibration. The total bandwidth of 856 MHz centered at 1283.9869 was split into 32,768 channels. In the vicinity of the redshifted H I 21-cm line frequency at $z = 0.029$ ($\sim 1380 \text{ MHz}$) the channel width corresponds to a velocity resolution of 5.7 km s^{-1} . The correlator dump time was 8 seconds and the data were acquired for all four polarization products, labelled XX, XY, YX and YY. Here, we are interested only in the Stokes-I properties of the target, therefore only XX and YY polarization products were processed through the Automated Radio Telescope Imaging Pipeline (ARTIP; see [Gupta et al. 2021](#), for details of processing steps).

The spectral line processing through ARTIP partitions the frequency band into 15 spectral windows (referred as SPW-0 to -14) with an overlap of 256 frequency channels. For the science objectives of this paper we consider only the continuum images and spectral line cubes from SPW-9 which covers 1351 - 1411 MHz. The spatial resolution of the continuum image obtained using ROBUST = 0 weighting of the visibilities in the CASA tclean task is $11''.6 \times 7''.0$ (position angle = -85.8°). The rms noise, measured close to quasar, in this image at the reference frequency of 1380.8 MHz is $\sim 80 \mu\text{Jy beam}^{-1}$. As expected (see Section 3.2), the quasar PKS 2020-370 is unresolved with a total continuum flux density of $404.1 \pm 1.1 \text{ mJy}$. The quoted flux density and the uncertainty are obtained un-

³ The National Radio Astronomy Observatory is a facility of the National Science Foundation operated under cooperative agreement by Associated Universities, Inc.

ing the single Gaussian component fitted to the continuum image. The typical error on flux density at these low frequencies is expected to be $\sim 5\%$.

We also generated a continuum subtracted image cube corresponding to SPW-9. For this we imaged only the central $34'$ centered at PKS2020-370, which is adequate to cover the galaxy group of interest. This **ROBUST** = 0 cube has 1024×1024 spatial pixels of size $2''$ and 2304 frequency channels (resolution $\sim 5.7 \text{ km s}^{-1}$). The image cube has a common restoring beam, i.e. spatial resolution of $11''.9 \times 7''.6$ ($6.9 \text{ kpc} \times 4.4 \text{ kpc}$ at z_{grp}) with a position angle of -82.7° , and the rms of $0.79 \text{ mJy beam}^{-1} \text{ channel}^{-1}$. The deconvolution of the line signal present in the image cube is done over two steps. First, we used the Common Astronomy Software Applications (CASA) package task **tclean** to deconvolve the signal down to five times the single channel rms. Then, we used the 3D source finding application, SoFiA 2⁴ (Serra et al. 2015; Westmeier et al. 2021) to identify the voxels with H I emission signal in the cube. This involved fitting a polynomial of order one to remove the residual continuum subtraction errors, and using the smooth + clip source finder with a combination of spatial kernels of 0, 3, 6, and 9 pixels and spectral kernels of 0, 3, 7, and 15 channels. A threshold of $3.5\sigma_{\text{rms}}$ and the reliability filter with reliability threshold of 0.95 were used to reject unreliable detections. The output three-dimensional SoFiA mask was then used to further deconvolve the signal down to the single channel rms. This cube was then corrected for the primary beam attenuation using the model from KAT-BEAM library⁵. The resultant cube was used for generating H I moment maps and further analysis. For moment-1 and moment-2 maps, we have used only those pixels where the signal was detected at 1.5 times the local rms.

3.2 uGMRT

The uGMRT observations were carried out on 2018 May 28 and 29, using a bandwidth of 4.17 MHz split into 512 channels. The total on-source time was 6.3 h. We also observed 3C 48 for flux density scale and bandpass calibrations. The compact radio source PKS1954-388 was also observed for 7 min every ~ 50 min. These observations were planned to complement the MeerKAT observation of PKS2020-370 carried out on 2017, November 7 and 9, using only 16 antennas from the array, with a single objective of detecting the absorption for verification purposes. These shallow MeerKAT observations are not discussed here, and mentioned only to clarify the motivation of uGMRT observations.

The uGMRT data were also reduced using ARTIP. The Stokes-*I* image made using **ROBUST** = 0 weighting of the visibilities has a restoring beam of $3''.9 \times 1''.8$ with a position angle of 29.4° . PKS2020-370 is compact at this resolution with a deconvolved size of $0''.7 \times 0''.1$ (position angle = $45 \pm 2^\circ$). The peak and total flux densities are $409.7 \pm 0.4 \text{ mJy beam}^{-1}$ and $419.3 \pm 0.8 \text{ mJy}$, respectively. The Stokes-*I* spectrum of the quasar has a resolution and spectral rms noise of 1.88 km s^{-1} and $1.7 \text{ mJy beam}^{-1} \text{ channel}^{-1}$, respectively.

4 RESULTS AND DISCUSSION

4.1 Klemola 31 group in H I emission

We detect H I 21-cm emission associated with four of the six members of the Klemola 31 galaxy group. In Fig. 1, we show the DSS *B_j*, *R*, and *I* color composite image exhibiting all the group members along with their names obtained from SIMBAD. Also, overlaid on the optical image are H I column density contours based on the MeerKAT data. The H I column density is calculated using:

$$\frac{N_{\text{HI}}}{\text{cm}^{-2}} = \frac{1.104 \times 10^{24} (1+z)^3}{b_{\text{maj}} \times b_{\text{min}}} \int \frac{I(v)}{\text{Jy beam}^{-1}} \frac{dv}{\text{km s}^{-1}}. \quad (1)$$

Here b_{maj} and b_{min} are major and minor axes of the restoring beam in arcseconds, and $\int I(v) dv$ is the total intensity in $\text{Jy km s}^{-1} \text{ beam}^{-1}$, with v being measured in the reference frame of the target. The spectral rms noise in the image cube for an assumed line width of 15 km s^{-1} corresponds to the 3σ H I column density of $3.1 \times 10^{20} \text{ cm}^{-2}$.

The H I emission from the group members resides in the frequency range of 1379.4 – 1382.2 MHz. This corresponds to the redshift (z_{HI}) and recession velocity ($v_o = cz_{\text{HI}}$) ranges of 0.0276 – 0.0297 and $8274.3 - 8903.8 \text{ km s}^{-1}$, respectively, estimated from the center of global H I emission profiles of individual galaxies. The H I masses are calculated using:

$$\frac{M_{\text{HI}}}{M_\odot} = \frac{2.356 \times 10^5}{1 + z_{\text{HI}}} \times \left(\frac{D_L}{\text{Mpc}} \right)^2 \int \frac{S(v)}{\text{Jy}} \frac{dv}{\text{km s}^{-1}}, \quad (2)$$

where D_L is the cosmological luminosity distance corresponding to z_{HI} . All the above mentioned properties, i.e., position, redshift, recession velocity, integrated line flux and H I mass are provided in rows 1 - 6 of Table 2. The 3σ upper limits on H I masses ($< 5 \times 10^8 M_\odot$) of galaxies undetected in H I emission, i.e., Klemola 31B and LEDA 2807038, have been estimated assuming a line width of 200 km s^{-1} .

As previously discussed, H I emission observations of Klemola 31A have been reported in the literature. The total line flux of $0.78 \text{ Jy km s}^{-1}$ reported by Boisse et al. (1988) is consistent with our MeerKAT measurement of $0.86 \pm 0.08 \text{ Jy km s}^{-1}$. Klemola 31A has the morphology of a barred ‘ocular’ spiral galaxy exhibiting oval shaped bright structure at the center and a double spiral arm on the side of the galaxy away from Klemola 31B (see also Fig. 8 of Carilli & van Gorkom 1992). The formation of such structures is very short-lived (one rotation) and is sensitive to the strength of tidal interaction (Elmegreen et al. 1991). The H I disk also resembles the warped structure with large reservoir of neutral hydrogen gas trailing the far-side spiral arms from the galaxy B indicating a recent tidal disruption. We return to this point in Section 4.2.

Among all four galaxies detected in H I emission, the most massive galaxy, ESO 400-11, is an edge-on spiral galaxy with total H I flux of $2.03 \pm 0.13 \text{ Jy km s}^{-1}$ and H I mass, $M_{\text{HI}} = 6.82 \times 10^9 M_\odot$. As is usual for disk galaxies, the H I disk extends well beyond the stellar disk. It also shows a disturbed morphology, and similar to Klemola 31A, has a gas poor ($M_{\text{HI}} < 1.57 \times 10^7 M_\odot$) early-type galaxy (LEDA 2807038) as a companion.

The most remarkable contrast between the stellar and H I components revealed by the MeerKAT imaging is observed for ESO 400-13, which is a S0 galaxy. The integrated H I emission line flux and the corresponding H I mass are

⁴ <https://github.com/SoFiA-Admin/SoFiA-2>

⁵ <https://github.com/ska-sa/katbeam>

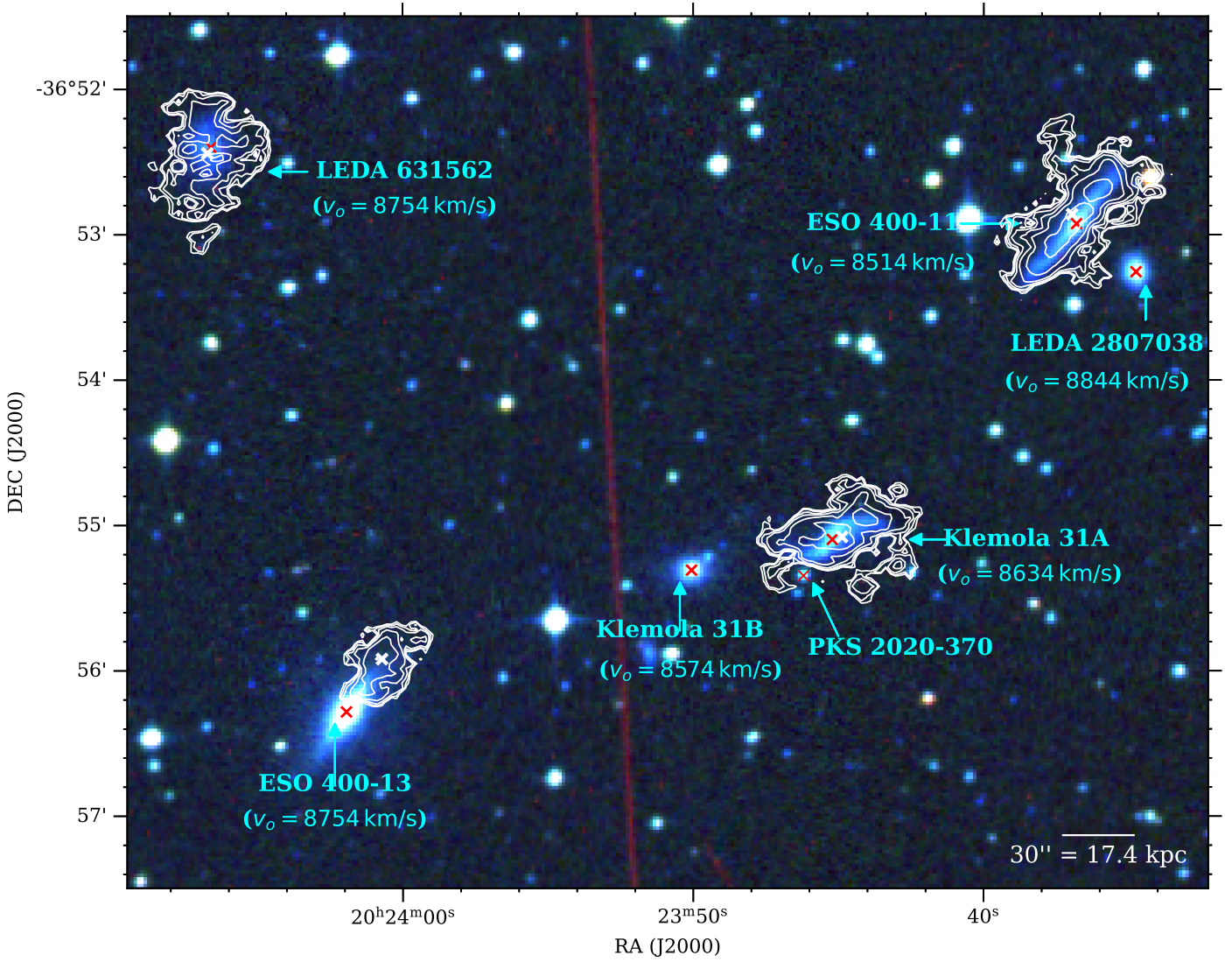


Figure 1. Klemola 31 group members and PKS 2020-370 shown in optical Digitized Sky Survey (DSS) B_j , R , and I color composite image with H I column density contours obtained from the moment-0 map. The contours correspond to H I column densities of $2^n \times 5 \times 10^{19} \text{ cm}^{-2}$ ($n = 0, 1, 2, 3, \dots$). The central positions of optical and H I disks are marked using red and white crosses, respectively. The recession velocity (v_0 in km s^{-1}) corresponding to z_g is denoted below the name of the galaxy. Note that only four of the six group members are detected in H I emission. The radio image has a restoring beam of $11''.9 \times 7''.6$ with a position angle of -82.7° .

$0.32 \pm 0.06 \text{ Jy km s}^{-1}$ and $1.06 \times 10^9 M_\odot$, respectively. Interestingly, the entire H I disk is systematically offset by $\sim 14 \text{ kpc}$ from stellar disk. Such segregation of H I from the optical disk has been observed in a few other cases. NGC4438 in the Virgo cluster core and Arp 105 are remarkable examples of displacement between H I gas and optical disks (Combes et al. 1988; Duc et al. 1997).

Lastly, the optically faint galaxy LEDA 631562 has H I flux of $0.40 \pm 0.07 \text{ Jy km s}^{-1}$ and the corresponding H I mass of $1.41 \times 10^9 M_\odot$. Curiously, the $[\text{N II}]/\text{H}\alpha$ versus $[\text{O III}]/\text{H}\beta$ ratios i.e., the Baldwin, Phillips, & Terlevich (BPT) diagnostic for this galaxy is consistent with ionization through a power-law spectrum, i.e., an active galactic nuclei (Chilingarian et al. 2017). The central AGN may also be responsible for the H I hole observed at the center of this galaxy. In passing, we

note that the BPT diagnostic is available for two other galaxies i.e., ESO 400-11 and ESO 400-13 from RCSED2⁶, and are consistent with these being normal star-forming galaxies. Only ESO 400-11 is clearly detected⁷ in radio continuum in the MALS wideband image (rms noise $\sim 30 \mu\text{Jy beam}^{-1}$) with a total flux density of 3.1 mJy . This implies a star formation rate (SFR) of $2.8 M_\odot \text{ yr}^{-1}$ (Bell 2003). ESO 400-13 is only tentatively detected in the radio continuum with a flux density of 0.4 mJy (SFR $\sim 0.6 M_\odot \text{ yr}^{-1}$).

Overall, Klemola 31 is a rare example of galaxy group at an early stage of its evolution with different morphologies

⁶ <https://rcsed2.voxastro.org/>

⁷ Excluding Klemola 31A which can not be reliably investigated in radio continuum due to the proximity of PKS 2020-370.

Table 2. Properties of Klemola group members based on H I 21-cm emission line

		ESO 400-11	ESO 400-13	Klemola 31A	LEDA 631562	Klemola 31B	LEDA 2807038
(1)	R.A.	20 ^h 23 ^m 36 ^s .96	20 ^h 24 ^m 0 ^s .72	20 ^h 23 ^m 44 ^s .88	20 ^h 24 ^m 6 ^s .72	20 ^h 23 ^m 50 ^s .16	20 ^h 23 ^m 34 ^s .8
(2)	Declination	−36° 52′ 51″.6	−36° 55′ 55″.2	−36° 55′ 4″.8	−36° 52′ 26″.4	−36° 55′ 19″.2	−36° 53′ 16″.8
(3)	$z_{\text{H I}}$	0.02867	0.02861	0.02872	0.02927	-	-
(4)	$v_{\text{H I}}$ (km s ^{−1})	8595	8577	8610	8776	-	-
(5)	S (Jy Km/s)	2.03 ± 0.13	0.32 ± 0.06	0.86 ± 0.08	0.40 ± 0.07	< 0.14	< 0.14
(6)	log $M_{\text{H I}}$ (M_{\odot})	9.86 ± 0.03	9.05 ± 0.09	9.50 ± 0.04	9.20 ± 0.08	< 8.7	< 8.7
(7)	MAJ _s	38.7″	19.2″	32.7″	24.6″	-	-
(8)	MIN _s	15.5″	11.8″	15.1″	18.7″	-	-
(9)	PA _s	−47.1°	−42.3°	−65.9°	−8.1°	-	-
(10)	D _{H I} (kpc)	44.7	23.4	38.0	28.8	-	-
(11)	D _{H I} /D ₂₅	1.04	0.56	1.21	1.34	-	-
(12)	log $M_{\text{H I}}^{\text{exp}}$ (M_{\odot})	9.98 ± 0.21	9.89 ± 0.21	9.72 ± 0.21	9.28 ± 0.21	9.17 ± 0.21	9.20 ± 0.21
(13)	DEF (M_{\odot})	0.12	0.84	0.22	0.08	-	-

and types of galaxies. Although we find recent gravitational disturbances in most of the individual galaxies, we do not detect any intra-group H I emission in the form of bridges and clumps. Nevertheless, the H I content and morphology of each galaxy in the group seems to be affected by the group environment or by interaction with other galaxies (e.g., see [Serra et al. 2013, 2015; Gupta et al. 2018](#)). These processes may lead to galaxies becoming H I deficient. In order to obtain the H I-deficiency we estimate the expected H I masses for all the member galaxies of Klemola 31 using the following scaling relation based on B-band luminosity ([Jones et al. 2018](#)):

$$\log [M_{\text{H I}}^{\text{exp}}/M_{\odot}] = X \log [L_{\text{B}}/L_{\odot}] + Y \quad (3)$$

where, X and Y are gradient and intercept estimated by [Jones et al. \(2018\)](#) for different morphological type galaxies. The B-band luminosity (L_{B}) is derived by

$$\log [L_{\text{B}}/L_{\odot}] = 10 + 2 \log [D_{\text{L}}/\text{Mpc}] + 0.4(M_{\text{bol},\odot} - B^{\text{c}}) \quad (4)$$

where, $M_{\text{bol},\odot} = 4.88$ is the bolometric absolute magnitude of the Sun ([Lisenfeld et al. 2011](#)), B^{c} is the corrected B-band magnitude after galactic extinction, internal extinction and k-correction. The B-band magnitude for all the galaxies are obtained from HyperLeda⁸.

The expected H I mass values ($\log M_{\text{H I}}^{\text{exp}}$) for the galaxies calculated using Eq. 3 are presented in Table 2. The deficiency parameter, i.e., the deficiency between expected H I mass and observed H I mass is defined as, $\text{DEF}_{\text{H I}} = \log M_{\text{H I}}^{\text{exp}}/M_{\odot} - \log M_{\text{H I}}/M_{\odot}$. A negative value of $\text{DEF}_{\text{H I}}$ parameter indicates H I excess in the galaxy whereas a positive value suggests H I deficiency. In the literature, to account for intrinsic scatter in the used scaling relations, the galaxies are usually considered to be H I deficient when $\text{DEF}_{\text{H I}} > 0.2$ –0.3 dex. Considering this, only ESO 400-13 shows significant H I deficiency ($\text{DEF}_{\text{H I}} = 0.84$). This is not surprising as this galaxy also shows the maximum displacement between the optical and H I disks (Fig. 1). The H I gas is totally asymmetric, being pushed on one side of the galaxy only. This is characteristic of a ram-pressure stripped galaxy, running at high velocity in a hot and tenuous intra-galactic gas (IGM).

Examples of H I detected in only one side of galaxies can be found in the Coma cluster ([Chen et al. 2020](#)). It is however

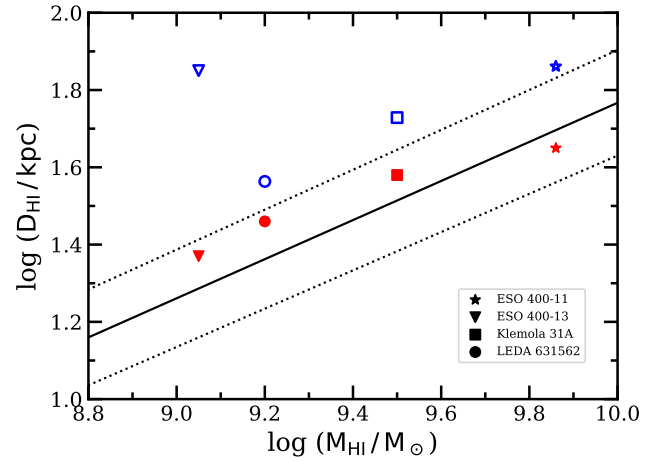


Figure 2. The $D_{\text{H I}} - M_{\text{H I}}$ relation for the detected galaxies. The red (filled) symbols are based on $D_{\text{H I}}$ and $M_{\text{H I}}$ based on our measurements. The blue (open) symbols use $D_{\text{H I}}$ predicted using the scaling relation based on optical diameter, D_{25} ([Broeils & Rhee 1997](#)). Each galaxy has been shown using a different symbol. The solid lines represent the best-fit linear relation from [Wang et al. \(2016\)](#) and the dashed line represents 3σ scatter.

unique in galaxy groups. Klemola 31 is a small group, and is not expected to contain a dense IGM, thus the ESO 400-13 galaxy must be crossing the group at very high velocity, mainly in the plane of the sky, since its redshift is comparable to the other group galaxies. For stripping to occur, the ram pressure on the H I needs to be greater than the restoring gravitational force. The ram-pressure (P_{ram}) as well as the anchoring self-gravity Π from ESO 400-13, can be modelled following [Gunn & Gott \(1972\)](#) as

$$P_{\text{ram}} = \rho_{\text{IGM}} v_{\text{gal}}^2, \text{ and} \quad (5)$$

$$\Pi = 2\pi G \Sigma_s \Sigma_g \quad (6)$$

Here, Σ_s and Σ_g are stellar and gas surface densities, respectively. The B-band magnitude and D_{25} of ESO 400-13 (Table 1), for a mass-to-light ratio of unity correspond to $\Sigma_s \approx 16 M_{\odot} \text{ pc}^{-2}$. Similarly, assuming that the galaxy prior to stripping had $M_{\text{H I}}^{\text{exp}}$ distributed over D_{25} , we get $\Sigma_g \approx$

⁸ <http://leda.univ-lyon1.fr>

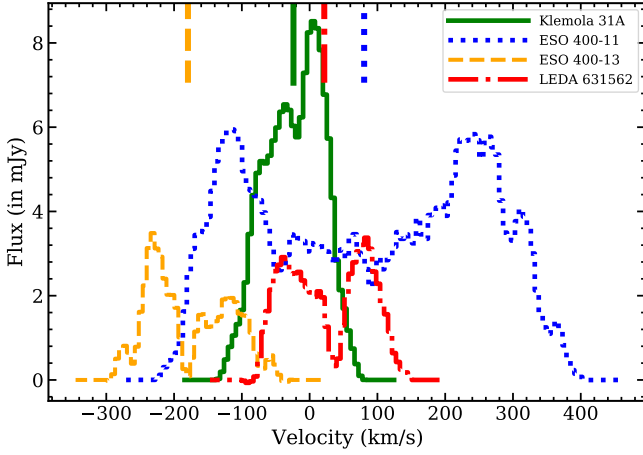


Figure 3. The global H I profiles of Klemola 31A, ESO 400-11, ESO 400-13 and LEDA 631562. The zero of the velocity scale is defined with respect to optical redshift, z_g (see Table 1). The dashed vertical lines denote z_{H1} .

$8 M_{\odot} \text{ pc}^{-2}$. If the gas is distributed over a larger area, as is typically the case, then it will be even more susceptible to stripping. For a typical density of hot gas ($3 \times 10^{-3} \text{ cm}^{-3}$) in the center of the group, the equations 5 and 6 imply a typical relative velocity of $\sim 200 \text{ km s}^{-1}$. This is totally feasible, and compatible with the hypothesis of ram pressure stripping for ESO 400-13.

We estimated the H I diameter (D_{H1}) of each galaxy by fitting ellipses to the H I column density contour map corresponding to $1 [M_{\odot} \text{ pc}^{-2}] = 1.25 \times 10^{20} \text{ cm}^{-2}$. For Klemola 31A, the estimated $D_{H1} = 38.02 \text{ kpc}$ is consistent with the value provided by Carilli & van Gorkom (1992). ESO 400-11 has the largest H I disk diameter of 44.7 kpc in the group, whereas, ESO 400-13 and LEDA 631562 have D_{H1} of only 23.4 kpc and 28.8 kpc, respectively. In Fig. 2, red (filled) symbols represent D_{H1} and M_{H1} based on our measurements. The solid lines represent the best-fit linear relation from Wang et al. (2016) and the dashed line represents 3σ scatter. Clearly, all group members detected in H I are in compliance with the relation. Only the expected H I-size of ESO 400-13 is strikingly larger than its measured size, and this supports the ram-pressure stripped character of this galaxy.

H I disks of galaxies are known to extend well beyond the optical disks by about a factor of ~ 2 (Broeils & Rhee 1997). The optical diameters i.e., D_{25} of the group members are provided in Table 1. We find the H I disks of Klemola group members to be significantly truncated with respect to their optical disks (see row 11 of Table 2). If the D_{H1} of these galaxies were truly representative of the D_{H1} - D_{25} scaling relation, $\log D_{H1} = (1 \pm 0.03) \log D_{25} + (0.23 \pm 0.04)$, from Broeils & Rhee (1997), the corresponding points would lie well above the D_{H1} - M_{H1} relation (shown with blue/open symbols in Fig. 2) Unsurprisingly, the most significant deviation is observed for ESO 400-13, an early-type galaxy with $D_{H1}/D_{25} = 0.56$. Similar deviations are also observed in the case of Virgo cluster spirals Cayatte et al. (1994). Reynolds et al. (2021) have also recently observed truncation of the H I disks of Hydra cluster galaxies compared to their field galaxy counterparts, and attribute this to earlier stages of losing H I

gas reservoirs likely as a result of environmental processes stripping the gas (e.g. ram pressure and tidal stripping). All this demands further investigation of gas removal processes in different environments which affect the D_{H1} - D_{25} relation, but leave the D_{H1} - M_{H1} relation remarkably intact (Stevens et al. 2019).

4.2 Galaxy group H I kinematics

The high spatial resolution capabilities of the MeerKAT allows for kinematics analysis of the group. Despite the disturbed H I morphology, all the galaxies are resolved above 3-beam elements along the projected major axis. Fig. 3 displays the global spectra of the four detected galaxies. The H I spectra have been centered on their optically-defined redshifts. Note that ESO 400-13 is detected only on the blue-shifted side. Klemola 31A and ESO 400-13 show kinematic asymmetry in comparison to the other two galaxies. The lopsided gas distribution of Klemola 31A and ESO 400-13 are clearly visible in Fig. 3. Such asymmetries can arise mainly due to three different environmental mechanisms, i.e., (1) galactic interaction, (2) gas accretion from neighbouring filaments and (3) ram-pressure stripping (e.g., Chung et al. 2007; Mapelli et al. 2008; de Blok et al. 2014; Dénes et al. 2016; Elagali et al. 2019). Our observations do not reveal any prominent H I bridge/tail that would arise from tidal interactions or minor mergers with neighbour galaxies. However, clear signature of ram pressure stripping are evident for ESO 400-13, which shows significant compressed H I gas (by factor of ~ 2) in the receding velocity side towards Klemola 31A.

The first three moments of the individual H I cubes, i.e., surface density, velocity field, and velocity dispersion, are plotted in Fig. 4. The velocity fields for three galaxies are only slightly perturbed by interactions, while the ram-pressure stripped ESO 400-13 has the most irregular spectrum and velocity field. Klemola 31A reveals a characteristic distortion in its SE extension, due to the competition between emission and absorption in front of PKS 2020-370. There is also a SW tidal extension, displaying receding velocities, suggesting that the tail is not in the same plane as the galaxy, dragged out by the interaction with Klemola 31B. ESO 400-11 reveals also tidal extensions, due to the action of LEDA 2807038. LEDA 631562 has the most regular velocity field, despite the central H I hole. ESO 400-13 reveals the characteristic perturbation of ram-pressure stripping, suggesting a high velocity with respect to the rest of the group, mainly in the plane of the sky. Only half of the H I velocity field is observed.

The velocity dispersions are in concordance with the findings of the velocity maps. There are only small perturbations with respect to the usual feature, of a maximum dispersion along the minor axis of galaxies, due to the strong gradient in this region of the spider diagram. Only for the ram-pressure stripped galaxy, ESO 400-13, where only one side is H I detected, and the minor axis is deficient, the dispersion map is unusual and strongly perturbed.

4.3 Line of sight absorption towards PKS 2020-370

The H I 21-cm absorption spectra towards the quasar are shown in Fig. 5. The GMRT spectrum presented in the top panel has been smoothed by 3 channels to obtain a

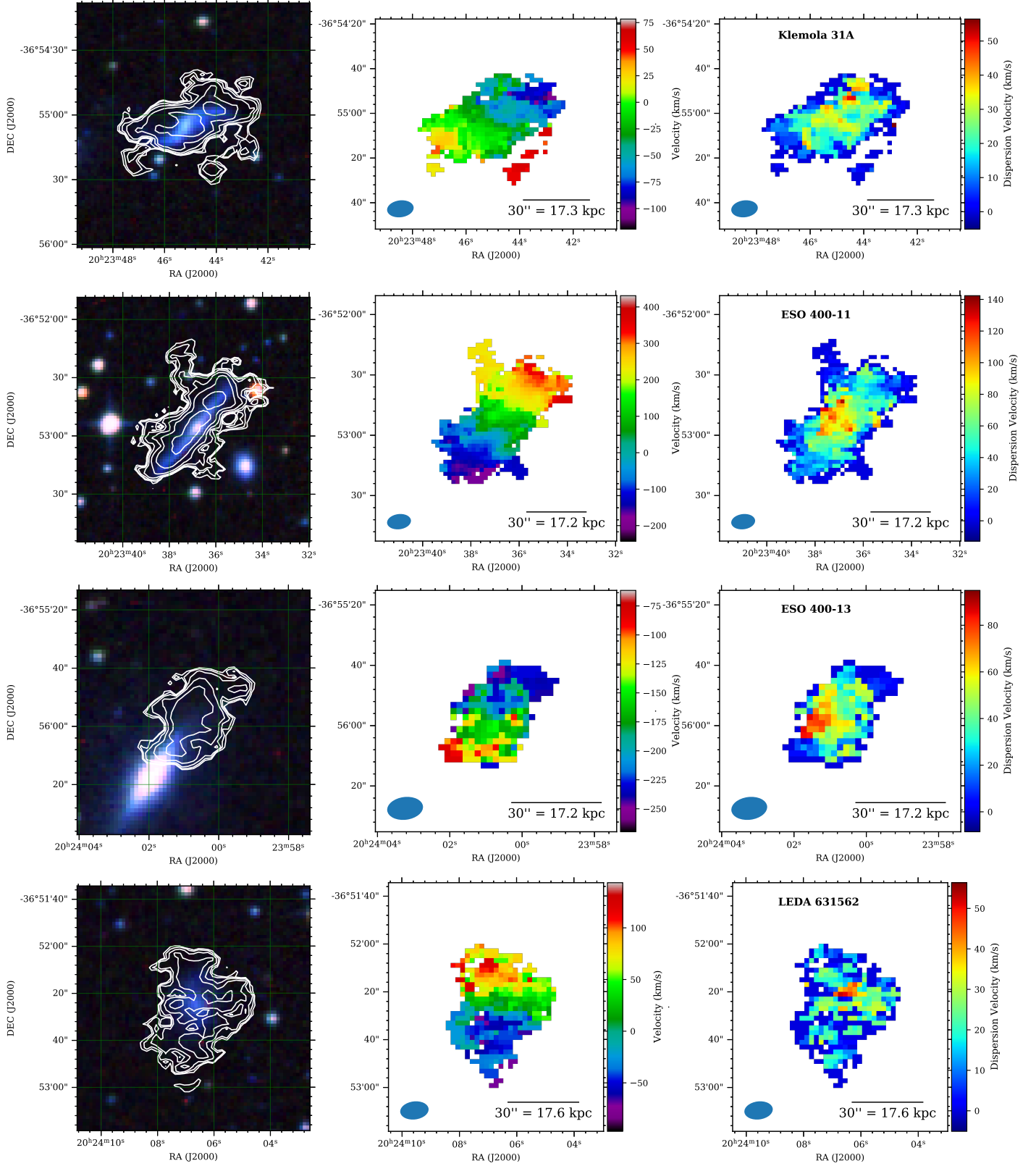


Figure 4. H I column density (moment-0) contours plotted over RGB cutouts from the optical DSS image (left), moment-1 maps (middle) and moment-2 maps (right) of four detected H I sources, Klemola 31A, ESO 400-11, ESO 400-13, and LEDA 631562. The zero of the velocity scales in middle panels are defined with respect to z_g based on the optical spectra (Table 1). The contours in the middle panels correspond to H I column densities of $2^n \times 5 \times 10^{19} \text{ cm}^{-2}$ ($n = 0, 1, 2, 3, \dots$). The MeerKat restoring beam of $11''.9'' \times 7''.6''$ ($6.9 \text{ kpc} \times 4.4 \text{ kpc}$) and a spatial scale bar of $30''$ are also shown in middle and right panels.

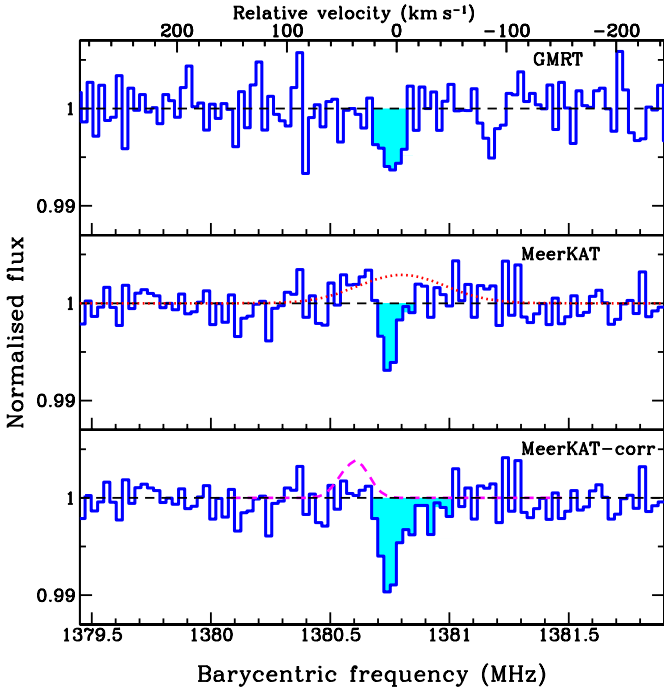


Figure 5. H I 21-cm absorption towards PKS 2020-370 (spectral resolution $\sim 5.7 \text{ km s}^{-1}$). The zero of the velocity scale is defined with respect to the peak of the absorption i.e., $z_{21\text{cm}} = 0.0287$. The dashed line in the middle panel represents the model for the H I emission. The bottom panel shows absorption profile corrected using this model (see text for details). Overplotted in magenta is a predicted emission line profile, based on the model of a regularly rotating disk. The model has been constructed by fitting a tilted-ring model to the data cube, as described in Sect. 4.3.

spectral resolution comparable to the MeerKAT spectrum ($\sim 5.7 \text{ km s}^{-1}$). The absorption signal in the MeerKAT spectrum is clearly contaminated by the H I emission (see middle panel of Fig. 5). This emission is much less evident in the GMRT spectrum but it is clear that the continuum subtraction is not perfect here as well. Simply using the frequency ranges marked by the shaded regions in the top and middle panels, we measure $\int \tau dv = 0.13 \pm 0.04 \text{ km s}^{-1}$ (GMRT) and $0.09 \pm 0.02 \text{ km s}^{-1}$ (MeerKAT), respectively. In both the cases, the unaccounted systematic error due to continuum subtraction dominates the optical depth estimate.

We focus on the more sensitive MeerKAT spectrum and correct the absorption profile for contamination from emission as following. First, we mask the frequency channels detected in absorption, shown as shaded region in the middle panel, in the MeerKAT spectrum. Next, we model the emission in the remaining channels using a single Gaussian component (see dotted line in the middle panel). The absorption profile corrected using this model is shown in the bottom panel of Fig. 5 and corresponds to $\int \tau dv = 0.26 \pm 0.03 \text{ km s}^{-1}$. Still, the uncertainties in determining the emission profile to use for the continuum subtraction would dominate. Nevertheless, the estimated integrated absorption matches well within 1σ with the VLA A-configuration measurement by Carilli &

van Gorkom (1987). Later in the section, we attempt to address the limitations of this simplistic approach.

For optically thin gas, the H I 21-cm optical depth is related to the H I column density, covering factor f_c and spin temperature T_s through

$$\frac{N(\text{H I})}{\text{cm}^{-2}} = 1.823 \times 10^{18} \frac{T_s}{\text{K}} \frac{1}{f_c} \int \tau(v) \frac{dv}{\text{km s}^{-1}} \quad (7)$$

PKS 2020-370 has a flat spectral index, $\alpha \approx 0.2$, over 0.8 - 20 GHz, and based on WISE mid-infrared colors can be classified as a blazar (D’Abrusco et al. 2019; Gupta et al. 2021). Both of these suggest that the radio emission is core-dominated. The milliarcsecond scale images at 2.3 GHz recover 85% of the total flux density (Petrov & Kovalev 2017), of which 90% is in the central ‘core-jet’ component with an extent of $0''.015$ (9 pc at $z_{\text{grp}} = 0.029$). The typical sizes of CNM clouds producing H I 21-cm absorption is > 5 pc and they may be part of cold gas structures that extend beyond ~ 35 pc (Gupta et al. 2018). Further, constraints on the covering factor can only be obtained through milliarcsecond scale resolution spectroscopy (see also Srikanth et al. 2013). Here, we proceed with the reasonable assumption of $f_c = 1.0$, and estimate $N(\text{H I}) = (4.7 \pm 0.6) \times 10^{19} (\frac{T_s}{100 \text{ K}}) (\frac{1.0}{f_c}) \text{ cm}^{-2}$. The H I emission model used to correct the MeerKAT absorption profile corresponds to $N(\text{H I}) = 1.4 \times 10^{21} \text{ cm}^{-2}$. For $\int \tau dv = 0.26 \pm 0.03 \text{ km s}^{-1}$, this corresponds to the limit, $T_s < 2950 \text{ K}$. Naturally, this is a conservative upper limit since H I emission is integrated over an area of $6.9 \text{ kpc} \times 4.4 \text{ kpc}$, and cannot be compared with absorption if there are inhomogeneities and clumpiness.

To estimate the H I column density, and derive the spin temperature of the H I, at the position of PKS 2020-370 in an alternative approach, we created a tilted-ring model, using a direct fit to the data cube. Such a model will also allow us to probe the line of sight velocity field probed by absorption in the framework of rotating HI disk. For this, we used a cutout of our data cube around the position of Klemola 31A, which is shown in Fig. 6. We then applied the tilted-ring modelling software FAT (Kamphuis et al. 2015) to get an initial tilted-ring model. In the following, TiRiFiC (Józsa et al. 2007), a computer program, which also optimises tilted-ring parameters through simulating spectroscopic 3-D data cubes of rotating galactic disks, was used to simplify this model. While FAT is a fully automated software and uses TiRiFiC as the underlying engine, TiRiFiC in the standalone mode allows for somewhat higher flexibility, in particular the sampling of the parameters at different intervals, a feature, which has been made use of in this study. The tilted-ring parameters surface brightness, rotation velocity, inclination and position angle were distributed on nodes at radii between $R = 0''$ and $R = 56''$ and automatically optimized. We use an Akima interpolation between the single nodes, while nodes at the edge of the disk (at radii $R = 0''$ and $R = 56''$) were chosen to assume the value of the closest node for the rotation velocity, the position angle, and the inclination. This implies that the rotation curve is approximately flat. The surface brightness was chosen to taper off to a value of 0 at the outermost radius $R = 56''$. The centre of the model, the systemic velocity, and the dispersion were fitted to be constant with radius. After attempting several combinations of parameters, and calculating errors as described in Józsa et al. (2021), we arrive at a slightly warped disk with a parametrization as shown in

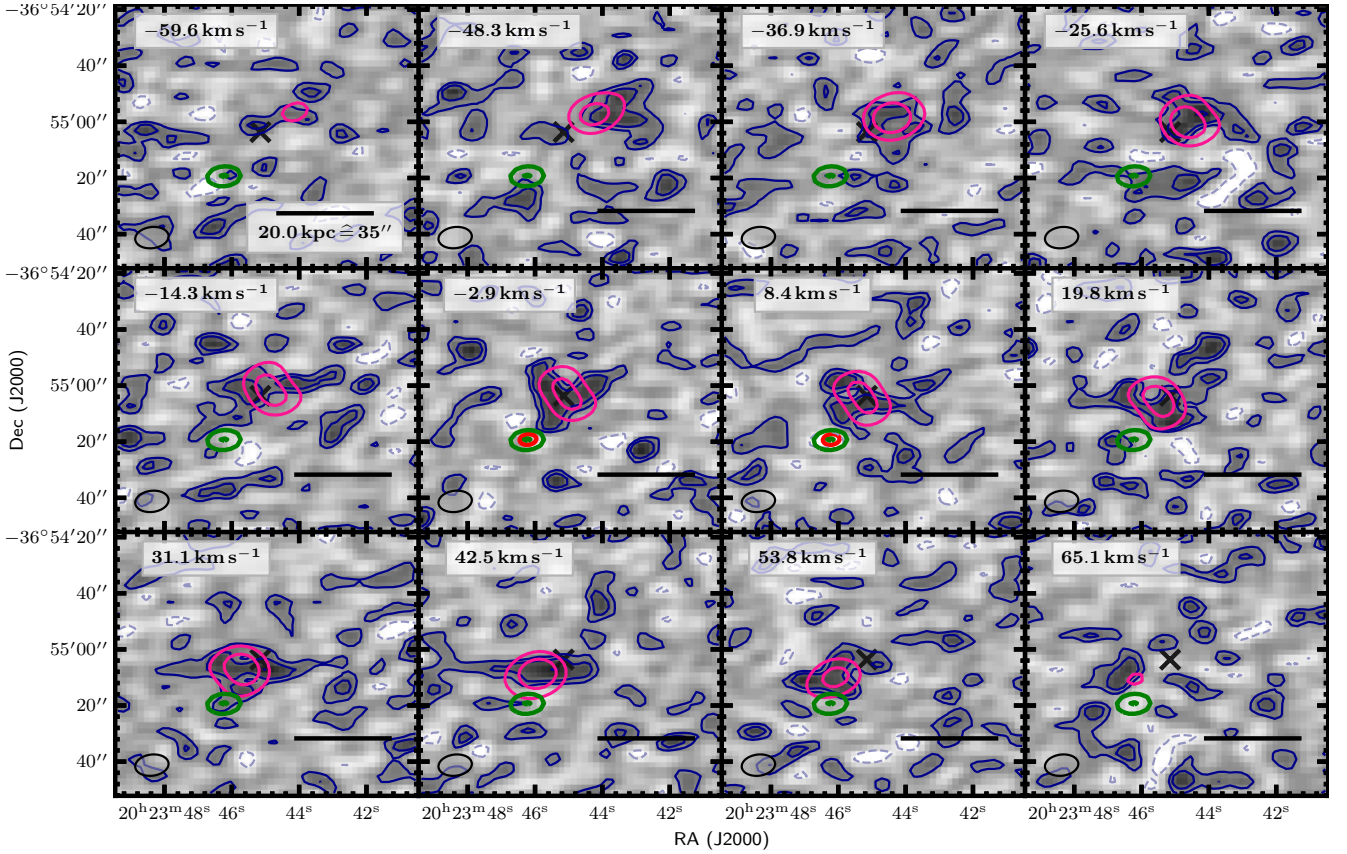


Figure 6. H I data cube resulting from the MeerKAT observations (blue contours and greyscale), TiRiFiC model data cube (pink contours), and continuum image of PKS 2020-370 (green contours). Every second channel of the data cube is shown. The velocity is measured relative to $z = 0.0287$ at the peak velocity of the absorption feature against PKS 2020-370. The red ellipses mark channels in the velocity range of the absorption feature ($FWHM \approx 16 \text{ km s}^{-1}$). Dark grey cross: centre of TiRiFiC model. Contours corresponding to line emission scale by $\sigma_{\text{rms}} = 0.79 \text{ mJy beam}^{-1}$. Light blue and dashed contours (MeerKAT data cube): $-2 \sigma_{\text{rms}}$. Blue and pink contours (MeerKAT data cube and TiRiFiC model): 1, 2, 4 σ_{rms} . Green contours (radio continuum): 200, 400 mJy beam^{-1} . The black ellipse in the lower left corners of the channel maps denotes the synthesized beam at half power.

Fig. 7. Fig. 6 shows model data cube overplotted on the original data. While the signal-to-noise ratio in the data cube is relatively high, owing to the high spectral resolution of the cube, we get a reasonable, albeit not perfect, match with the data. Fig. 8 shows the column density map of the original data and the model. Here also, it is evident that the data are not reproduced perfectly. Accepting the corresponding uncertainties, we obtain an H I emission line model at the position of PKS 2020-370 at our hands, which we next compare to the observed absorption profile.

To predict the column density and the velocity of H I gas at the location of PKS 2020-370 from our model without being hampered by beam smearing effects, we created a model data cube at a very high spatial resolution (pixel size of $0.2''$ and a half-power-beam-width of $0.6''$). Next we created a column-density map and obtain the column density of $N(\text{H I}) = 2.5 \times 10^{20} \text{ cm}^{-2}$ at the location of the PKS 2020-370. For $N(\text{H I}) = 2.5 \times 10^{20} \text{ cm}^{-2}$ and $\int \tau dv = 0.26 \text{ km s}^{-1}$, we can then calculate the corresponding $T_s = 530 \text{ K}$ for a homogeneous regularly rotating disk. This result relies solely on the assumption that the morphology is reflected by our tilted-ring model, and does not take the kinematics into account.

Next, we make use of the kinematical model to estimate whether the absorption profile indeed arises from a regularly

rotating disk. The predicted corresponding H I emission profile is shown in the bottom panel of Fig. 5. The emission peak, corresponding to $N(\text{H I}) = 2.5 \times 10^{20} \text{ cm}^{-2}$, has a dispersion of 12.9 km s^{-1} and is offset with respect to absorption peak by 38.0 km s^{-1} ($z_{21\text{cm}} = 0.0287$). The observed absorption profile hence stems from gas, which is not participating in the (assumed) regular rotation of the disk, it is anomalous gas. This can also be seen directly from the data cube (Fig. 6). At the velocity of the absorption feature against PKS 2020-370, the peak of the emission has a significant offset from the position of the background source (Fig. 6, central panels). The absorption line feature has hence a velocity corresponding to the systemic velocity, but not corresponding to the receding (South-East) portion of the disk, which would be expected according to our simple model: the absorption would occur at the edge of the receding side of the disk (Fig. 6, central bottom panels).

To further explore the gas distribution along the line of sight, we obtained the Keck/HIRES (High Resolution Echelle Spectrometer) raw data of PKS 2020-370 from Keck Observatory Archive (KOA)⁹. We processed the raw data using IRAF

⁹ <https://koa.ipac.caltech.edu/>

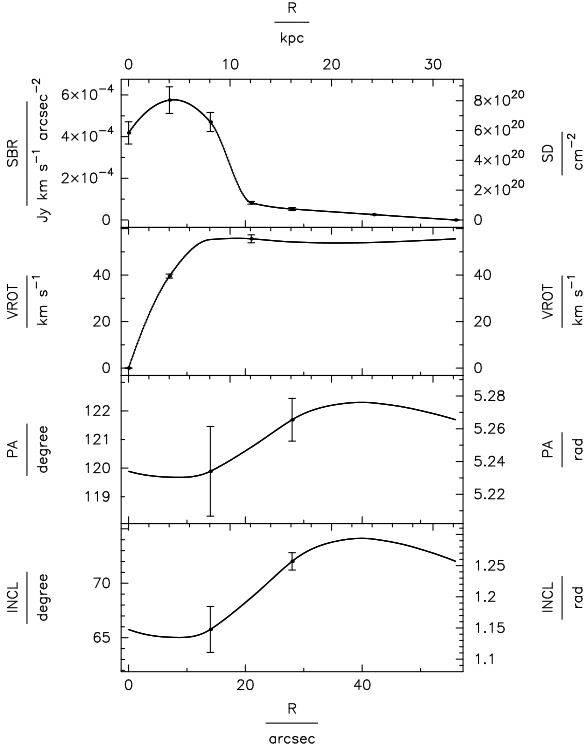


Figure 7. TiRiFiC tilted-ring model of the H I disk of Klemola 31A. The curves are spline fits, the edge points having the same value as the last data point for each parameter. SBR: surface brightness. SD: surface column density. VROT: rotation velocity. PA: position angle. INCL: inclination.

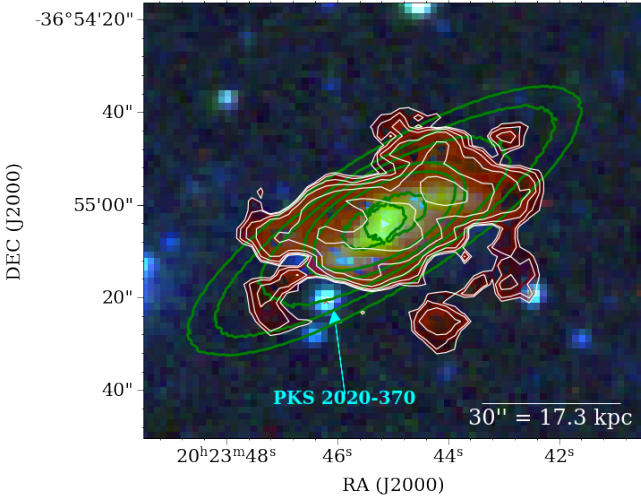


Figure 8. Observed moment-0 map of Klemola 31A in autumn color gradient (increasing $N(\text{H I})$ from brown to yellow) overlaid on the RGB cutout of DSS image. We also show the observed (white) and TiRiFiC tilted-ring model (green) moment-0 contours with the same levels as Fig. 4.

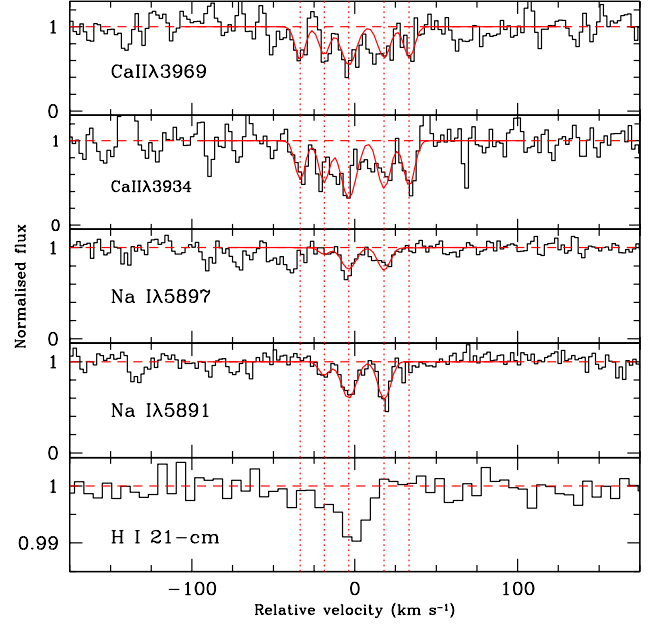


Figure 9. Comparison of the absorption profiles Ca II, Na I and H I 21-cm absorption associated with Klemola 31A towards PKS 2020-370. The best fitted Voigt profiles (components identified with red vertical dotted lines) are over-plotted. The zero velocity scale is defined at $z_{\text{abs}} = 0.028725$.

to obtain the continuum normalized spectrum, and identified the Ca II and Na I metal lines associated with Klemola 31A (see also [Junkkarinen & Barlow 1994](#)). We fitted Voigt profiles to the metal absorption lines using [VPFIT](#)¹⁰. In this case we assume the b-parameter to be same for Na I and Ca II. We show the absorption profile and best-fitted Voigt profiles in Fig. 9, and present the Doppler parameter (b) and the column density of the fitted components in Table 3. From Fig. 9, we can see the Ca II absorption is spread over $\sim 80 \text{ km s}^{-1}$ (between -40 to $+40 \text{ km s}^{-1}$ with respect to $z_{\text{abs}} = 0.028725$) in 5 distinct components. Na I absorption is clearly detected in the three central components two of them coinciding with the H I 21-cm absorption. The measured velocity spread clearly supports the presence of additional gas components (with anomalous velocities) compared to the H I disk.

The observed Na I/Ca II ratios are consistent with what is typically seen in gas producing 21-cm absorption in quasar-galaxy pairs where the line of sight does not pass through the gaseous or stellar disk ([Dutta et al. 2017](#)). In the Milky Way, we typically observe $N(\text{Na I}) > N(\text{Ca II})$ (see Fig. 9 of [Welty et al. 1996](#)). Thus, it appears that the Ca depletion is unlike what we see in the cold ISM (i.e., about 3 orders of magnitude). Since Na I is not shielded to ionizing radiation it is possible that the low Na I/Ca II ratio towards PKS2020-370 reflects low radiation field as compared to the Galactic background radiation ([Dutta et al. 2017](#)). Thus, based on kinematics and the line ratio discussed above it appears most of the absorption is produced by gas unrelated to cold H I disk.

¹⁰ <http://www.ast.cam.ac.uk/~rfc/vpfit.html>

Table 3. Metal absorption components of Klemola 31A toward PKS 2020-370.

z_{abs}	b	$\log N(\text{Ca II})$	$\log N(\text{Na I})$	Notes
(1)	(in km s^{-1})	(in cm^{-2})	(in cm^{-2})	(5)
0.028661	2.02 ± 1.77	12.08 ± 0.26	11.12 ± 0.11	Tied- b
0.028713	4.47 ± 0.70	12.32 ± 0.09	11.76 ± 0.04	Tied- b
0.028787	3.21 ± 0.70	12.15 ± 0.11	11.74 ± 0.04	Tied- b
0.028611	1.12 ± 1.10	12.44 ± 1.25	–	
0.028840	2.16 ± 1.73	12.14 ± 0.26	–	

There are two possibilities to explain the anomalous velocity of the absorption feature. Firstly, it might come from anomalous gas in the disk. Streaming motions due to the spiral arms, and velocity perturbations due to tidal interaction could cause the offset. In this case, the column-density estimate from the tilted-ring model and with that the estimate of $T_s = 530$ K might still be valid. However, given a maximal rotation velocity of 56 km s^{-1} and an estimated projected rotation velocity of 53 km s^{-1} (for an inclination of 72°), the offset of 38 km s^{-1} is significant, and the occurrence of such strong streaming motions along spiral arms for lower-mass galaxies might be more difficult to justify. Alternatively, the gas seen in absorption might not come from the disk.

Overall, our observations may also indicate an extraplanar origin of the gas. In this case the spin temperature would remain an unknown, as we would not have a good measure of the H I column density in emission. The H I tidal extension to Klemola 31A towards the SW (see Sect. 4.2) might provide an explanation of the occurrence of the extraplanar gas in the sight line of the quasar. Assuming a tidal stream of H I debris occurring between Klemola 31A and Klemola 31B, with the observed tidal extension to Klemola 31A being the sole visible part, any part of a hypothetical stream should have a velocity between the systemic velocity of Klemola 31B and the tidal feature. Klemola 31B is blueshifted with respect to the absorption line and the observed tidal feature redshifted. Our observations hence would not stand in contrast to the hypothesis of the origin of the absorption feature being tidal debris from an interaction between Klemola 31A and Klemola 31B. As our estimate of T_s is based on a model of a homogeneous, circularly symmetric disk, and we know that the galaxy group, and with it, Klemola 31A undergoes tidal interactions, we can only take these results as an indication. An independent estimate of $N(\text{H I})$ through ultraviolet spectroscopy will help to derive the harmonic mean temperature along the line-of-sight (e.g., Keeney et al. 2005).

5 SUMMARY AND CONCLUSIONS

The wide field of view and large instantaneous bandwidth of the MeerKAT array permits the simultaneous completion of several investigations requiring sensitive H I 21-cm emission and absorption, and radio continuum imaging. Our aim was to identify with high spatial resolution the interstellar medium responsible for the H I absorption in front of the quasar PKS 2020-370. Located in the outer parts of the H I disk of Klemola 31A, the line of sight reveals both emission and absorption, perturbing significantly the derived H I surface density and velocity field of the foreground galaxy.

Out of the six identified galaxies of the Klemola 31 group, in the MeerKAT field of view, four are detected and well resolved in H I. Three of them are only slightly perturbed, two through tidal interactions with small companions. They reveal tidal extensions, and out of the plane velocities, but not significant gas depletion. The fourth one, ESO 400-13 is strongly H I-deficient, and reveals a totally asymmetric H I distribution, characteristic of ram-pressure stripped galaxies. The H I is detected only on the approaching side of the galaxy. This is suggesting that the galaxy is crossing the group with a high velocity, mainly in the plane of the sky.

Using symmetry arguments and tilted-ring modelling of Klemola 31A, we derive for the gas absorbing in front of PKS2020-370 a spin temperature of $T_s = 530$ K under the assumption that the absorption arises from a symmetric disk. This rather high value, unexpected for a disk, as well as the velocity offset of the absorption feature from the expected radial velocity of the disk model, might indicate an extraplanar origin of the absorption feature. One explanation could be that we observe tidal debris, as the galaxy group is in a rather dynamical state, as indicated by asymmetric kinematics and morphology of the group members. The same interaction, however, might be responsible for a deviation of the kinematics of Klemola 31A from the assumed circularity of orbits, in which case the discrepancy of the velocities might be due to streaming motions.

This work demonstrates that the MALS large program, dedicated to absorption studies, will lead to environmental studies in galaxy groups through their H I emission mapping, and help in understanding the origins of gas responsible for H I 21-cm absorption.

ACKNOWLEDGEMENTS

We thank MeerKAT and GMRT staff for their support during the observations. We also thank the referee for helpful comments. The MeerKAT telescope is operated by the South African Radio Astronomy Observatory, which is a facility of the National Research Foundation, an agency of the Department of Science and Innovation. GMRT is run by the National Centre for Radio Astrophysics of the Tata Institute of Fundamental Research. This research has made use of the Keck Observatory Archive (KOA), which is operated by the W. M. Keck Observatory and the NASA Exoplanet Science Institute (NExSci), under contract with the National Aeronautics and Space Administration. The MeerKAT data were processed using the MALS computing facility at IUCAA (<https://mals.iucaa.in/releases>).

DATA AVAILABILITY

The data used in this work are obtained using MeerKAT (SSV-20180516-NG-02) and GMRT (ddtC003). The raw data will become available for public use in accordance with the observatory policy. The MeerKAT data products will be publicly released through the survey website: <https://mals.iucaa.in>.

REFERENCES

- Bell E. F., 2003, *ApJ*, **586**, 794
- Boettcher E., et al., 2022, arXiv e-prints, p. [arXiv:2202.04669](#)
- Boisse P., Dickey J. M., Kazes I., Bergeron J., 1988, *A&A*, **191**, 193
- Boksenberg A., Danziger I. J., Fosbury R. A. E., Goss W. M., 1980, *ApJ*, **242**, L145
- Borthakur S., Momjian E., Heckman T. M., York D. G., Bowen D. V., Yun M. S., Tripp T. M., 2014, *ApJ*, **795**, 98
- Broeils A. H., Rhee M. H., 1997, *A&A*, **324**, 877
- Cappellari M., et al., 2011, *MNRAS*, **416**, 1680
- Carilli C. L., van Gorkom J. H., 1987, *ApJ*, **319**, 683
- Carilli C. L., van Gorkom J. H., 1992, *ApJ*, **399**, 373
- Castignani G., et al., 2022, *A&A*, **657**, A9
- Cayatte V., Kotanyi C., Balkowski C., van Gorkom J. H., 1994, *AJ*, **107**, 1003
- Chen H., et al., 2020, *MNRAS*, **496**, 4654
- Cherinka B., Schulte-Ladbeck R. E., 2011, *AJ*, **142**, 122
- Chilingarian I. V., Zolotukhin I. Y., Katkov I. Y., Melchior A.-L., Rubtsov E. V., Grishin K. A., 2017, *ApJS*, **228**, 14
- Chung A., van Gorkom J. H., Kenney J. D. P., Vollmer B., 2007, *ApJ*, **659**, L115
- Combes F., Dupraz C., Casoli F., Pagani L., 1988, *A&A*, **203**, L9
- D’Abrusco R., et al., 2019, *ApJS*, **242**, 4
- Dénes H., Kilborn V. A., Koribalski B. S., Wong O. I., 2016, *MNRAS*, **455**, 1294
- Dressler A., 1980, *ApJ*, **236**, 351
- Duc P. A., Brinks E., Wink J. E., Mirabel I. F., 1997, *A&A*, **326**, 537
- Dutta R., Gupta N., Srianand R., O’Meara J. M., 2016, *MNRAS*, **456**, 4209
- Dutta R., Srianand R., Gupta N., Momjian E., Noterdaeme P., Petitjean P., Rahmani H., 2017, *MNRAS*, **465**, 588
- Elagali A., et al., 2019, *MNRAS*, **487**, 2797
- Elmegreen D. M., Sundin M., Elmegreen B., Sundelius B., 1991, *A&A*, **244**, 52
- Gerin M., Combes F., Athanassoula E., 1990, *A&A*, **230**, 37
- Gunn J. E., Gott J. Richard I., 1972, *ApJ*, **176**, 1
- Gupta N., et al., 2016, in MeerKAT Science: On the Pathway to the SKA. p. 14 ([arXiv:1708.07371](#))
- Gupta N., et al., 2018, *MNRAS*, **476**, 2432
- Gupta N., et al., 2021, *ApJ*, **907**, 11
- Healey S. E., et al., 2008, *ApJS*, **175**, 97
- Hotan A. W., et al., 2021, *PASA*, **38**, e009
- Irwin J. A., 1994, *ApJ*, **429**, 618
- Jarvis M., et al., 2016, in MeerKAT Science: On the Pathway to the SKA. p. 6 ([arXiv:1709.01901](#))
- Jonas J., MeerKAT Team 2016, in Proceedings of MeerKAT Science: On the Pathway to the SKA. 25-27 May, 2016 Stellenbosch, South Africa (MeerKAT2016). p. 1
- Jones M. G., et al., 2018, *A&A*, **609**, 1
- Józsa G., Kenn F., Klein U., Oosterloo T., 2007, *A&A*, **468**, 731
- Józsa G. I. G., et al., 2021, *MNRAS*, **501**, 2704
- Junkkarinen V. T., Barlow T. A., 1994, in American Astronomical Society Meeting Abstracts. p. 13.05
- Kamphuis P., Józsa G. I. G., Oh S. . H., Spekkens K., Urbancic N., Serra P., Koribalski B. S., Dettmar R. J., 2015, *MNRAS*, **452**, 3139
- Keeney B. A., Momjian E., Stocke J. T., Carilli C. L., Tumlinson J., 2005, *ApJ*, **622**, 267
- Klemola A. R., 1969, *AJ*, **74**, 804
- Koribalski B. S., et al., 2020, *Ap&SS*, **365**, 118
- Kulkarni S. R., Heiles C., 1988, Neutral hydrogen and the diffuse interstellar medium. pp 95–153
- Lisenfeld U., et al., 2011, *A&A*, **534**, A102
- Maddox N., et al., 2021, *A&A*, **646**, A35
- Mapelli M., Moore B., Bland-Hawthorn J., 2008, *MNRAS*, **388**, 697
- Peterson B. A., Jauncey D. J., Wright A. E., Condon J. J., 1976, *ApJ*, **207**, L5
- Petrov L., Kovalev Y. Y., 2017, *MNRAS*, **467**, L71
- Reeves S. N., et al., 2016, *MNRAS*, **457**, 2613
- Reynolds T. N., et al., 2021, *MNRAS*, **510**, 1716
- Serra P., et al., 2013, *MNRAS*, **428**, 370
- Serra P., et al., 2015, *MNRAS*, **452**, 2680
- Serra P., et al., 2016, in MeerKAT Science: On the Pathway to the SKA. p. 8 ([arXiv:1709.01289](#))
- Srianand R., Gupta N., Rahmani H., Momjian E., Petitjean P., Noterdaeme P., 2013, *MNRAS*, **428**, 2198
- Stevens A. R. H., Diemer B., Lagos C. d. P., Nelson D., Obreschkow D., Wang J., Marinacci F., 2019, *MNRAS*, **490**, 96
- Wang J., Koribalski B. S., Serra P., van der Hulst T., Roychowdhury S., Kamphuis P., Chengalur J. N., 2016, *MNRAS*, **460**, 2143
- Wang J., et al., 2021, *ApJ*, **915**, 70
- Welty D. E., Morton D. C., Hobbs L. M., 1996, *ApJS*, **106**, 533
- Westmeier T., et al., 2021, *MNRAS*, **506**, 3962
- Yun M. S., Ho P. T. P., Lo K. Y., 1994, *Nature*, **372**, 530
- de Blok W. J. G., et al., 2014, *A&A*, **569**, A68

This paper has been typeset from a \LaTeX file prepared by the author.